

SD-GAN: Structural and Denoising GAN reveals facial parts under occlusion

Samik Banerjee, Sukhendu Das

Dept. of CS&E, IIT Madras, Chennai, India

Abstract

Certain facial parts are salient (unique) in appearance, which substantially contribute to the holistic recognition of a subject. Occlusion of these salient parts deteriorates the performance of face recognition algorithms. In this paper, we propose a generative model to reconstruct the missing parts of the face which are under occlusion. The proposed generative model (SD-GAN) reconstructs a face preserving the illumination variation and identity of the face. A novel adversarial training algorithm has been designed for a bimodal mutually exclusive Generative Adversarial Network (GAN) model, for faster convergence. A novel adversarial "structural" loss function is also proposed, comprising of two components: a holistic and a local loss, characterized by SSIM and patch-wise MSE. Ablation studies on real and synthetically occluded face datasets reveal that our proposed technique outperforms the competing methods by a considerable margin, even for boosting the performance of Face Recognition.

Keywords: GAN, structural loss, Nash equilibrium, occlusion, PMSE, Face Verification

1. Introduction

Faces appearing under occlusion is a major hindrance for accurate Face Recognition (FR), which has been far from being solved. With the advent of generative adversarial models [1] in the field of deep learning (DL), there has been a surge of techniques to predict the missing values or pixels in an image. Revealing of missing parts of an image is a common image editing operation, which aims to fill

Email addresses: samik.banerjee.howrah@gmail.com (Samik Banerjee),
sdas@iitm.ac.in (Sukhendu Das)

the missing or masked regions in images with appropriate contents that appears to be visually realistic. The generated contents can either be as accurate as the original, or simply fit well within the context such that the restored image looks perceptually plausible and complete. Recent image completion techniques [2, 3] rely on low and mid-level cues for the generation of the missing patches in the image.

Contrary to the recent techniques, our proposed method reconstructs a full face despite the fact that certain salient and unique features on the faces are occluded. The processes concerned with generating missing patches on the faces make an assumption that the similar patterns do not exist everywhere. Inline with his assumptions, Generative Adversarial Networks (GANs) aim to perform well in generating the facial parts behind the mask, due to its capability of generating the unseen. Wright *et al.* [4] used a method for sparse recovery of signals for image completion, which is further used in face completion. Recently, Ren *et al.* [5] used Convolutional neural networks (CNN) for inpainting of images. Li *et al.* [6] used a generative model to restore face-parts occluded by patches on the CelebA dataset, but they did not provide any result on real-world occluded face datasets, like the AR face database [7]. They also relied on post-processing of the images to produce semantically correct images. The Generative Face Completion (GFC) [6] process requires significantly large amount of training time to reach the equilibrium point.

With the aim of designing an end-to-end framework for generating face images from the masked ones, the primary contribution of this paper lies in design of a novel bimodal training algorithm for GAN. Mode-I of the training process produces faces with ambient illumination, while Mode-II denoises that generated by Mode-I. A unique training algorithm is proposed with faster convergence. An adversarial "structural" loss is also proposed in this paper in order to maintain the holistic quality of the face images. This "structural" loss consists of two components: "Structural Similarity (SSIM) loss" and "Patch-wise Mean squared error (PMSE)". The SSIM [8] takes care of the holistic features of the face, while PMSE takes care of the pixel-wise differences in the faces. Further, our model converges to an equilibrium in Mode-II faster than other generative models [9], since the generator is based on a denoising auto-encoder [10] model. The generated faces boost the performance of FR on occluded faces, when compared with the works published recently in literature.

Sections 2 and 3 give brief overviews of GAN and Denoising Auto-encoder, respectively, while section 4 discusses the loss functions used in this paper. Section 5 gives the details of the proposed architecture of SD-GAN, followed by the

description of the proposed training algorithm in section 6. In section 7, the quantitative and qualitative results of our experiments, showing the effectiveness of our proposed method are reported, along with the different benchmark datasets used for experimentations. Finally, the paper concludes in section 8.

2. Generative Adversarial Networks (GAN)

Generative Adversarial Network (GAN) [1] consists of two models: the generative (G) and the discriminator (D). The CNN based deep network in G captures the true data distribution, p_{data} , and generates images sampled from a distribution p_z , the distribution of the training data provided as input to G . D as a counter-part of G (also CNN-based) discriminates between the original images, sampled from p_{data} , and the images generated by G . Typically, G learns to map from a latent space (p_z) to a particular data distribution (p_{data}) of interest, while D discriminates between instances from p_{data} and candidates produced by the generator. The objective of training G is to increase the error rate of D (i.e., "fool" D by producing novel synthesized instances that appear to have come from p_{data}). This adversarial training adopted for GAN is derived from that in Schmidhuber [11]. In other words, an alternate training procedure is performed on GAN, where D and G play a two-player minimax gaming strategy of a zero-sum game with the value function $V(G, D)$. The overall objective function minimized by GANs [1], is given as:

$$\min_G \max_D V(G, D) = \mathbb{E}_{x \sim p_{data}} [\log D(x)] + \mathbb{E}_{x \sim p_z} [\log(1 - D(G(z)))] \quad (1)$$

To learn p_z over data x , a mapping to data space is represented as $G(z; \theta_g)$, where G is a differentiable function representing a CNN with parameters θ_g . Another CNN based deep network represented by $D(x; \theta_d)$ outputs a single scalar $[0/1]$. $D(x)$ represents the probability that x came from the true data rather than p_z .

Two major drawbacks of an adversarial system are:

1. GANs can generate all the pixels in one shot, rather than guessing the value of one pixel given another pixel. This is the main reason for the noise in the output images, whenever missing pixels are generated.
2. Reaching the Nash equilibrium [12] of a game requires large number of iterations/epochs due to the instability inherent in GANs [1].

An aim to overcome the above two drawbacks, forms the basic motivation of our work presented in this paper. To deal with noise, a Denoising Auto-encoder based generator model has been introduced in conjunction with the standard GAN framework. Further, the Mode-II reaches the Nash equilibrium faster than Mode-I. A trade-off has been done at Mode-I between the structural loss and training time, where the generator loss is thresholded for the generated images passed to Mode-II for denoising.

3. Denoising Auto-encoder

The general deep auto-encoder, as proposed by Bengio *et al.* [13], maps an input vector $\vec{x} \in [0, 1]^d$ to a latent representation $\vec{y} \in [0, 1]^{d'}$ through a deterministic mapping $\vec{y} = f_\theta(x) = s(\mathbf{W}\vec{x} + \vec{b})$ with $\theta = \{\mathbf{W}, \vec{b}\}$, and then maps back to the reconstructed vector, $\vec{z} = g_{\theta'}(y) = s(\mathbf{W}'\vec{y} + \vec{b}')$, $\vec{z} \in [0, 1]^d$ in the input space with $\theta' = \{\mathbf{W}', \vec{b}'\}$, where $s(\cdot)$ denotes the activation function. The optimization of the parameters is based on the mean reconstruction error [13]:

$$\begin{aligned} \theta^*, \theta'^* &= \arg \min_{\theta, \theta'} \frac{1}{n} \sum_{i=1}^n L(\vec{x}^{(i)}, \vec{z}^{(i)}) \\ &= \arg \min_{\theta, \theta'} \frac{1}{n} \sum_{i=1}^n L(\vec{x}^{(i)}, g_{\theta'}(f_\theta(\vec{x}^{(i)}))) \end{aligned} \quad (2)$$

where, $\vec{x}^{(i)}$ represents the i^{th} training sample and L is the squared error $L(\vec{x}, \vec{z}) = \|\vec{x} - \vec{z}\|^2$.

Vincent *et al.* [10] designed a denoising autoencoder by modifying the formulation in equation 2. The authors assumed $\tilde{\vec{x}}$ to be a noisy approximation of \vec{x} , characterized by a stochastic mapping $\tilde{\vec{x}} \sim q_D(\tilde{\vec{x}}|\vec{x})$. The joint distribution is given as $q^0(\vec{x}, \tilde{\vec{x}}, \vec{y}) = q^0(\vec{x})q_D(\tilde{\vec{x}}|\vec{x})\delta_{f_\theta(\tilde{\vec{x}})}(\vec{y})$, where $\delta_u(v) = 0$, when $u \neq v$, and parameterized by θ . Thus, \vec{y} becomes the deterministic function of $\tilde{\vec{x}}$. The objective function in equation 2 thus transforms into:

$$\arg \min_{\theta, \theta'} \mathbb{E}_{q^0(\vec{x}, \tilde{\vec{x}})} [L(\vec{x}^{(i)}, g_{\theta'}(f_\theta(\tilde{\vec{x}}^{(i)})))] \quad (3)$$

Patch-wise minimization of mean-squared error (discussed later in section 4.3) further helps in image denoising [14]. Thus patch-wise mean squared error loss has been used in this paper as a component of the loss function in both the generators (G_1 & G_2) of our SD-GAN framework.

4. Loss Functions

The process of training the SD-GAN consists of two modes, and optimizes four adversarial loss functions described (later) in equations 9-12. The corresponding criteria are described in the following sub-sections.

4.1. Binary Cross Entropy Loss

Binary cross-entropy is a loss function used effectively in the field of deep learning for binary classification problems and sigmoid output units. The binary class labels used at the discriminators are 0 & 1, representing the real and fake (generated) images. The loss function is given as:

$$\begin{aligned}\mathcal{L}_{bce}(\vec{y}, \vec{\tilde{y}}) &= -\frac{1}{n} \sum_{i=1}^n [y_i \log(\tilde{y}_i) + (1 - y_i) \log(1 - \tilde{y}_i)] \\ &= -\frac{1}{n} \sum_{i=1}^n \sum_{j=1}^m y_{ij} \log(\tilde{y}_{ij})\end{aligned}\tag{4}$$

where, i indexes n samples/observations and j indexes m classes, and y_i is the sample label (binary for LHS, one-hot vector on the RHS) and the prediction of sample is $\tilde{y}_{ij} \in (0, 1) : \sum_j \tilde{y}_{ij} = 1, \forall i, j$.

4.2. SSIM Loss

SSIM [8] gives the structural similarity index between two images (x_1 and x_2). We first define SSIM index [8], estimated using multiple patches (windows) of an image. This measure between two windows p and q of common size $N \times N$ is:

$$SSIM(p, q) = \frac{(2\mu_p\mu_q + c_1)(2\sigma_{pq} + c_2)}{(\mu_p^2 + \mu_q^2 + c_1)(\sigma_p^2 + \sigma_q^2 + c_2)}\tag{5}$$

where, μ_p, μ_q are the pixel-wise averages of image patches p and q respectively, σ_p^2, σ_q^2 their respective variances, σ_{pq} the covariance of p and q ; $c_1 = (k_1 L)^2$, $c_2 = (k_2 L)^2$ as two variables used to stabilize the division with weak denominator, L the dynamic range of the pixel-values (typically this is $2^{\#bits/pixel} - 1$), and $k_1 = 0.01$ and $k_2 = 0.03$ set by default. The SSIM loss (\mathcal{L}_{ssim}) function estimated between two single-channel (gray-scale) images, produces a maximum value of 1 for two identical images and decreases henceforth as the similarity between the images decreases. Hence, the SSIM loss is calculated as:

$$\mathcal{L}_{ssim} = 1 - SSIM(x_1, x_2)\tag{6}$$

where, SSIM is given in equation 5. Minimization of this loss provides a better estimate of the x_2 for x_1 .

4.3. Patch-wise MSE Loss

Patch-wise MSE (PMSE) loss is derived as the mean-squared error between two images. Let h_1 and h_2 be the two patches extracted from x_1 and x_2 , respectively. The PMSE between x_1 and x_2 , is calculated as:

$$\mathcal{L}_{pmse}(x_1, x_2) = \sum_{i=1}^{|C|} \frac{\lambda_i}{|h|} \sum_{j=1}^{|h|} \|h_1^{(i,j)} - h_2^{(i,j)}\|^2 \quad (7)$$

where, $|C|$ & $|h|$ are the number of channels and patches in an image, while h_k is a patch extracted from x_k and λ_i 's are the channel-wise weights of the image ($\lambda = \{0.2989, 0.5870, 0.1141\}$ as given in [15]). A weighted linear combination (using λ) of the MSE's is used to estimate the MSE of each patch. PMSE is the average MSE over all the pair of corresponding (spatially) patches in the images.

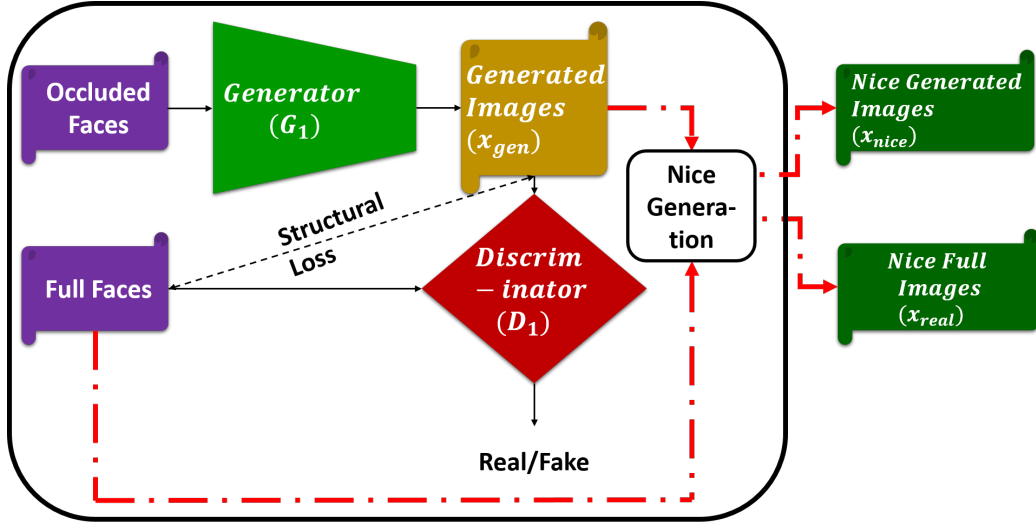
4.4. Structural Loss

This paper also proposes a novel structural loss (\mathcal{L}_{st}) in addition to the binary cross-entropy loss as in DCGAN [1]. The primary aim of proposing this novel loss is to constrain the structure of the generated image. The SSIM (see section 4.2) loss accounts for the facial structure while a mean-squared error (MSE) based loss applied patch-wise (refer section 4.3) helps to replicate of the illumination variation in G_1 and denoising in the auto-encoder based G_2 . The structural loss is given as:

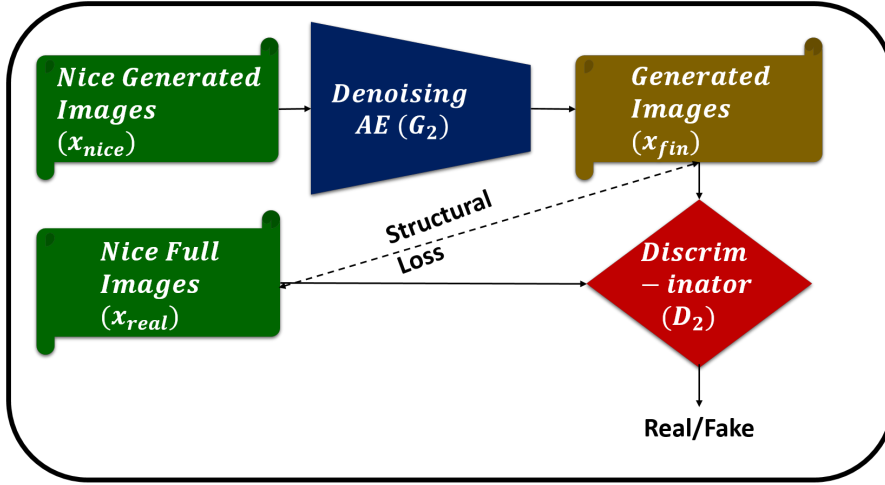
$$\mathcal{L}_{st} = \frac{\mathcal{L}_{ssim} + \mathcal{L}_{pmse}}{2} \quad (8)$$

5. The proposed architecture: SD-GAN

The proposed Structural and Denoising Generative Adversarial Network (SD-GAN) works in two-modes. Figures 1 & 2 show the proposed architecture with structural details of SD-GAN, and descriptions for each of the modes of operation are described in the following sub-sections.

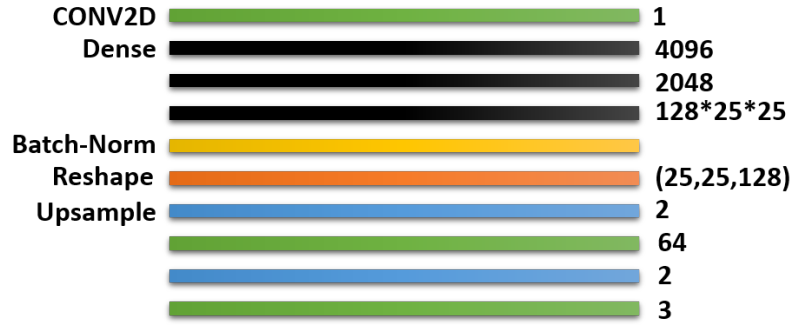


(a) Mode - I



(b) Mode - II

Figure 1: The proposed SD-GAN architecture (best viewed in color), exhibiting two modes of operations (training): (a) Mode - I and (b) Mode - II.



(a) Generator (G_1)



(b) Discriminator (D_1/D_2)



(c) Denoising AE (G_2)

Figure 2: Architectural Details of the CNN-based Generator and Discriminator used in SD-GAN (best viewed in color).

5.1. Mode-I

The Mode-I of SD-GAN is derived from DC-GAN [16], with a few variations in the input as well as in the training procedure (see section 6 for further details). The generator, G_1 , is a deep-network (see figure 2(a)) which takes the occluded faces as input, instead of the noise vector (as in DC-GAN) and generates (synthetic) faces to be fed to the discriminator D_1 . D_1 , similar to the discriminator network in DC-GAN (see figure 2(b)), takes both the full real-world facial as well as x_{gen} as inputs and attempts to discriminate between the real and generated (fake) images.

A "nice generation" module acts as an interface for selective data transfer between two modes of training. It takes fake images (x_{gen}) as input with a mini-batch of size 20, and computes a loss function (see line 5 of algorithm 1) to filter and create nice images (x_{nice}), when the loss is significantly low (< 0.01). The corresponding full face images are also filtered as x_{real} and given to mode-II of training. This is done under the assumption that G_1 has successfully fooled D_1 for the batch of images, when loss is low. Since x_{nice} are often corrupted by noise, an operation of denoising is necessary as done by mode-II of operation.

5.2. Mode-II

The Mode-II is the denoising unit of our proposed architecture, compared to the Mode-I which preserves the structural identity of the face. To perform the task of denoising, a denoising auto-encoder (see section 3) is used as the generator (G_2) in this mode of operation. For the CNN-based denoising auto-encoder (refer figure 2(c)) proposed in this paper, the generated "nice" images (x_{nice}) obtained from Mode-I are taken as inputs. The discriminator (D_2), identical to D_1 , takes as input x_{real} images and performs adversarial training independently and exclusively. Though the input to Mode-II is given as output of Mode-I, the training and weight update of the model at Mode-II is independent of the training of Mode-I, *i.e.* the gradients do not backpropagate into the model of Mode-I.

6. Training SD-GAN

The bimodal SD-GAN model is trained using the proposed algorithm 1. The procedure involves an end-to-end training of both the modes simultaneously. Each mode is trained using a procedure adopted from DC-GAN [16], with a structural loss induced for each mode, exclusively. The model is trained in *Keras* with *Tensorflow* backend [17]. A uniform mini-batch size of 20 samples has been used

throughout the training process, with gradient based optimization for weight update in the network. The following sub-sections detail the mode-wise training procedure, with the loss functions involved for weight update in the network (for all notations used hereafter, refer algorithm 1).

6.1. Training for Mode-I

The training process used for Mode-I is outlined in lines 4 – 12 of algorithm 1. The occluded images are given as inputs to G_1 , to generate fake images matching the underlying true distribution of the full-facial images. The semi-supervised training procedure of SD-GAN involves a discriminator D_1 to distinguish between the real-world and generated images. The full-faces corresponding to each of the occluded faces in a batch, B , is fed to the discriminator as real images. The training of D_1 is based on the minimization of the binary cross-entropy loss (\mathcal{L}_{bce}) (see section 4.1 for details), using the ADAM [18] optimizer. Let, x_{real} represent the set of full real-world face images and x_{occ} be the occluded faces in a particular batch, while $D_1(x, y)$ represents the discriminator function with an input x and a target label y (set as 1 for x_{real} and 0 for x_{occ}), and $G_1(x)$ depicts the generating function with the input x . The adversarial loss corresponding to D_1 can be written as:

$$\begin{aligned} \mathcal{L}_{D_1}^{adv}(x_{real}, x_{occ}) = \\ \mathcal{L}_{bce}(D_1(x_{real}, y), \vec{1}) + \mathcal{L}_{bce}(D_1(G_1(x_{occ}), y), \vec{0}) \end{aligned} \quad (9)$$

Training the generator G_1 is essentially an optimization process executed using Stochastic Gradient Descent (SGD) [19], while freezing the weight update of D_1 . The proposed structural loss (auxiliary) is induced at this stage of training. The adversarial loss for G_1 is:

$$\begin{aligned} \mathcal{L}_{G_1}^{adv}(x_{occ}, x_{real}) \\ = \mathcal{L}_{bce}(D_1(G_1(x_{occ}), y), \vec{1}) + \mathcal{L}_{st}(x_{real}, G_1(x_{occ})) \end{aligned} \quad (10)$$

where, \mathcal{L}_{st} is defined in equation 8.

Minimization of these two criteria given by equations (9) and (10), makes G_1 outsmart (by cheating) D_1 upon reaching Nash equilibrium [20], where D_1 believes that the images generated by G_1 is sampled from the true distribution.

6.2. Training for Mode-II

The output images obtained from Mode-I are used in training for Mode-II in SD-GAN. Hence, these batch of "nice" images (x_{nice}) generated by G_1 are

Algorithm 1: Overall training algorithm for SD-GAN

Input: Masked Face Image (F_m); Full Face (F_f)
Output: Trained models $\rightarrow \{D_1, G_1, D_2, G_2\}$

```
1  $B :=$  mini-batch from  $F_m$  &  $F_f$ 
2  $x_{nice} \leftarrow []$ ;  $x_{real} \leftarrow []$ 
3 while  $epoch \leq 100000$  do
4   foreach  $F_m^B$  in  $B$  do
5     //  $F_m^B \in F_m$  in batch  $B$ 
6     //  $F_f^B \in F_f$  in batch  $B$ 
7     Compute  $\mathcal{L}_{D_1}^{adv}(F_f^B, F_m^B)$  using equation 9 & minimize
8      $D_1.trainable := \text{False}$ 
9     Compute  $\mathcal{L}_{G_1}^{adv}(F_m^B, F_f^B)$  using equation 10 & minimize
10     $D_1.trainable := \text{True}$ 
11    if  $x_{loss} \leq 0.01$  then
12       $x_{nice} := \text{append}(x_{nice}, x_{gen})$ 
13       $x_{real} := \text{append}(x_{real}, F_f^B)$ 
14    end
15    if  $x_{nice}$  is not empty then
16       $B_n :=$  mini-batch from  $x_{nice}$  &  $x_{real}$ 
17      foreach  $N_m^B$  in  $B_n$  do
18        //  $N_m^B \in x_{nice}$  in batch  $B_n$ 
19        //  $O_f^B \in x_{real}$  in batch  $B_n$ 
20        Compute  $\mathcal{L}_{D_2}^{adv}(O_f^B, N_m^B)$  using equation 11 & minimize
21         $D_2.trainable := \text{False}$ 
22        Compute  $\mathcal{L}_{G_2}^{adv}(N_m^B, O_f^B)$  using equation 12 & minimize
23         $D_2.trainable := \text{True}$ 
24      end
25    end
26  end
27   $epoch := epoch + 1$ 
28 end
```

/* $D.trainable = \text{FALSE}$ indicates that the weights are frozen, and when TRUE weight update is performed using Backpropagation. */

provided as inputs to Mode-II along with their corresponding (subject-wise) full-face images (x_{real}). Though, these images have their structural content partly preserved, they suffer from few degradation due to noise. To denoise these images, a denoising auto-encoder based generator model had been proposed in this paper. Lines 14 – 20 in algorithm 1 outlines mode-II of training. The Discriminator D_2 comprises of a similar adversarial loss as in D_1 , given as:

$$\begin{aligned} \mathcal{L}_{D_2}^{adv}(x_{real}, x_{nice}) = \\ \mathcal{L}_{bce}(D_2(x_{real}, y), \vec{1}) + \mathcal{L}_{bce}(D_2(G_2(x_{occ}), y), \vec{0}) \end{aligned} \quad (11)$$

The denoising auto-encoder training of G_2 is incremental, in a sense that the number of training samples increases as the G_1 becomes stronger. The instability issues [1] prevalent in training is taken care by over-training the weaker of the two to reach the equilibrium point. The adversarial loss incurred at this phase mainly deals with closing the gap between the distributions of the real and the generated (fake) samples. The adversarial loss at G_2 is given by:

$$\begin{aligned} \mathcal{L}_{G_2}^{adv}(x_{nice}, x_{real}) = \\ \mathcal{L}_{bce}(D_2(G_2(x_{occ}), y), \vec{1}) + \mathcal{L}_{aux}(x_{real}, G_1(x_{occ})) \end{aligned} \quad (12)$$

where,

$\mathcal{L}_{aux} = \Delta(\mathcal{L}_{st}(x_{real}, G_1(x_{occ})), \mathcal{L}_{st}(x_{real}, G_2(x_{nice})))$, and Δ being the difference operator.

Minimization of $\mathcal{L}_{G_2}^{adv}$ reduces the gap in structural and pixel-values between the generated (fake) and true samples, which also reduces the noise in the generated samples.

The use of Mode-II of training along with Mode-I (done independently) reduces the overall time for training ($\sim 10^2$ folds, considering the number of epochs) compared to a recent state-of-the-art technique [6] used for the task at hand.

7. Results and Performance Analysis

This section first describes the datasets used, then gives the quantitative measures used to show the effectiveness of our proposed model for face completion and FR, compared with a few state-of-the-art techniques.

7.1. Datasets

Experimentations are carried on three datasets: (a) AR dataset [7], (b) Celeb-A dataset [21], and (c) multi-PIE [22]; each is briefly described below.

7.1.1. AR Database

The AR database [7] consists of face images which contain real-world occlusions. The database consists of 136 subjects with varying illumination conditions and expressions. For our study, we consider those images which are near-frontal and have minimal expression variations (see figure 3 for samples). Two variations of occlusions are available in the database, *viz.* the sunglasses and scarf on the face, which prevents the faces to be reconstructed using symmetric transformations from the other half of the face. For our experimentations, the dataset has been divided into 2 subsets: **AR1**, the images with sunglasses and **AR2**, those with scarfs. A data partition as 60 : 20 : 20 ratio is maintained uniformly for training, validation, and testing throughout the set of the experimentations. The subjects used for training and validation are never used for testing.

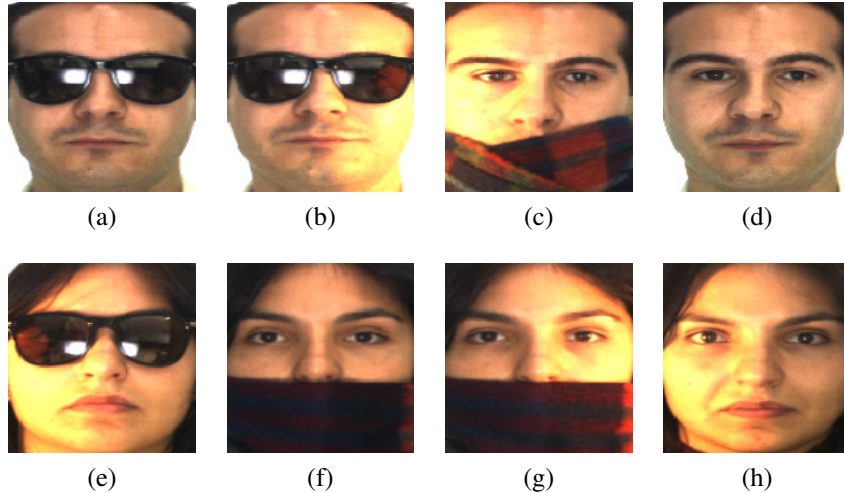


Figure 3: Two face image examples from AR database (one in each row) with different levels of occlusions and illumination variations. Images in $\{(a), (b), (e)\} \in \mathbf{AR1}$; while $\{(c), (f), (g)\} \in \mathbf{AR2}$; and $\{(d), (h)\}$ are the full face images (best viewed in color).

7.1.2. Celeb-A Database

The CelebA [21] dataset consists of 202,599 face images. Each face image is cropped, roughly aligned by the position of two eyes, and rescaled to $100 \times 100 \times 3$ pixels. The standard benchmark split with 162,770 images for training, 19,867 for validation and 19,962 for testing, has been followed for experimentation. A mask of size 50×50 pixels covers the face (see figure 4 for samples) at random locations, as described in [6].

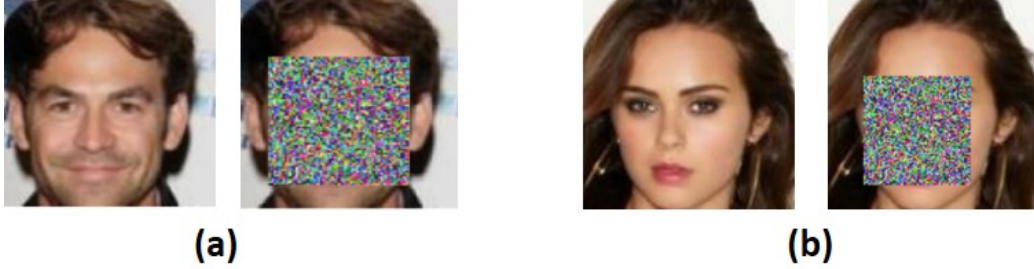


Figure 4: Examples from CelebA database, showing two subjects with synthetic occlusions (best viewed in color).

7.1.3. Multi-PIE dataset

The CMU Multi-PIE database [22] consists of 755,370 images shot in 4 different sessions from 337 subjects. The images in the dataset are split up into training, validation and test set. The training set is composed of all individuals in non-frontal pose (except those used for validation and testing) at the generator, while the size of the validation (64 identities at a pose of 90°) and test sets (65 identities at a pose of 90°) are almost identical. We consider the images taken in session 1, with the probe images taken at 90° pose.

7.2. Evaluation metrics

Along with the visual results shown in section 7.3 we perform quantitative evaluation of the proposed model for the two datasets under test. Firstly, we use the peak-signal-to-noise-ratio (PSNR) value, which captures the difference in the pixel values of the two images. PSNR (higher the better) is defined as:

$$\begin{aligned}
 MSE(x_{fin}, x_{real}) &= \frac{1}{mn} \sum_{i=1}^{m-1} \sum_{j=1}^{n-1} [x_{gen}(i, j) - x_{real}(i, j)]^2 \\
 PSNR &= 10 \cdot \log_{10} \left(\frac{MAX_{x_{fin}}^2}{MSE} \right)
 \end{aligned} \tag{13}$$

where, x_{fin} is the output (generated) image and x_{real} is the reference (ground-truth, GT) image.

Secondly, SSIM index (refer equation 5) is used for quantifying the generated results, which estimates the holistic similarity between two images. Finally, we

also use the identity distances measured by the OpenFace toolbox [23] to determine the high-level semantic similarity of two faces.

7.3. Performance Analysis for generation of full facial images

A few examples of generation of the full facial images from occluded faces are shown in figure 5 under two different scenarios of the proposed method. The column (b) depicts the output of DC-GAN [16], while the results progressively becomes better as we move towards the right, showing the effectiveness of the auxiliary losses proposed in this paper. The significant improvement in the image quality measure shown by our model in (e) as compared to (d) (see table 1 for quantitative measures showing similar trends) strengthens our claim for the introduction of Mode-II for denoising the output of Mode-I.

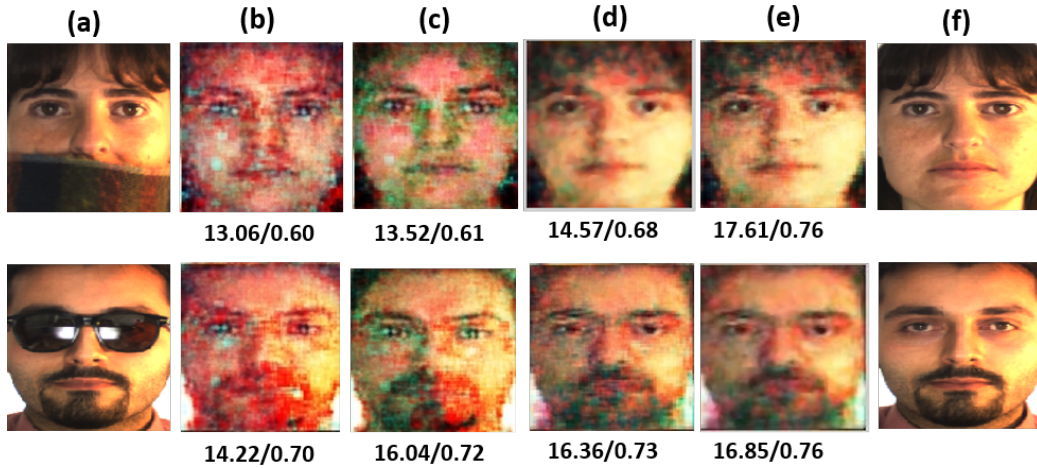


Figure 5: Results for image generation from two different sets of occlusions, *viz.*, **AR2** and **AR1** (arranged row-wise) present in AR, by SD-GAN: (a) the input occluded image, (b) output of G_1 using \mathcal{L}_{bce} , (c) output of G_1 using $\mathcal{L}_{bce} + \mathcal{L}_{ssim}$, (d) output of G_1 at Phase-I, (e) output of G_2 at Phase-II, (f) Ground-truth (GT). The values below each image from (b)-(e) give the (PSNR/SSIM) values of the images compared to the expected output (GT).

Both the quantitative as well as the qualitative measures are compared with a recent state-of-the-art technique. GFC [6] uses face parsing as well as Poisson Blending [24] as post-processing techniques to generate facial parts under occlusion. Graph Laplacian (GL) based methods [25] also attempts to solve the problem. The quantitative results evaluating the quality of the images are given in table 1. Our proposed SD-GAN (referred as 'SDG' in tables) outperforms all

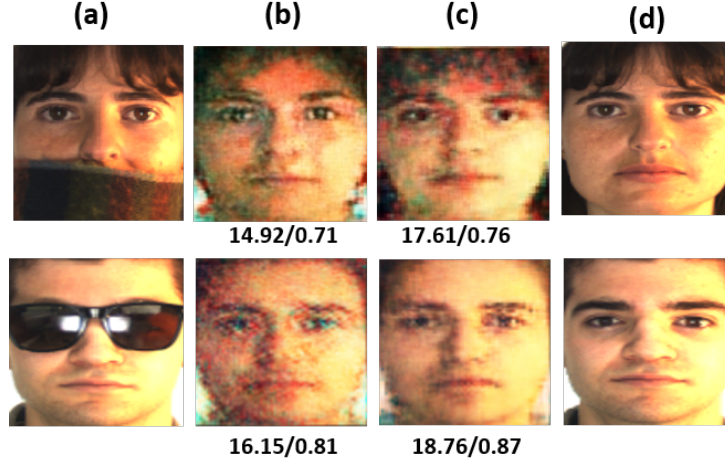


Figure 6: Results for image generation from two different methods: (a) occluded images (one each from **AR2** (*Top-row*) and **AR1** (*Bottom-Row*)), (b) Images generated by GFC [6] without post-processing, (c) Images generated by SD-GAN, (d) expected output. The values below each image gives the (PSNR/SSIM) values of the images compared to the expected output.

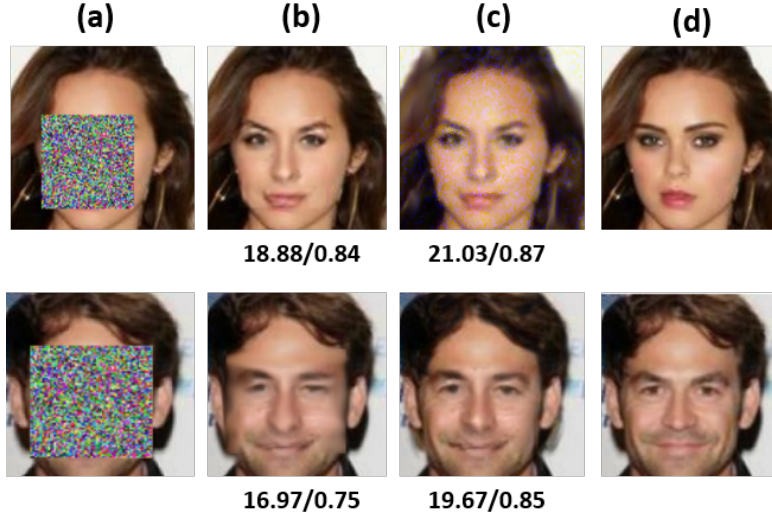


Figure 7: Results for image generation from two different methods: (a) occluded images (from Celeb-A dataset [21]), (b) Images generated by GFC [6] without post-processing, (c) Images generated by SD-GAN, (d) expected output. The values below each image gives the (PSNR/SSIM) values of the images compared to the expected output.

other techniques based on PSNR values, whereas in case of the holistic measure (SSIM), the nearest competing method GFC, also a GAN based deep model with post-processing techniques, matches our performance in a few cases and even marginally outperforms our proposed technique in only one case. Qualitative experiments also reveal that without the post-processing technique, GFC fails to match the performance of our proposed technique in both the datasets, for which our method is a clear winner, as shown in figures 6 & 7. The values at the bottom of the images in columns (b) & (c) in figures 6 & 7, reveal the superiority of our proposed SD-GAN, based on the PSNR/SSIM values on the four exemplar images.

Table 1: Quantitative values (averaged over the whole dataset) for different face images generated following the protocol, as in columns (b)-(d) of figure 5 for the AR dataset, compared with state-of-the-art techniques.

<i>Average PSNR Values</i> (higher the better)						
	(b)	(c)	(d)	GL	GFC	SDG
<i>AR1</i>	12.15	13.27	15.62	13.48	15.83	18.43
<i>AR2</i>	11.92	12.58	14.87	11.78	13.84	17.68
<i>CelebA</i>	12.31	12.86	16.82	9.43	18.30	18.61
<i>Average SSIM Indices</i> (higher the better)						
	(b)	(c)	(d)	GL	GFC	SDG
<i>AR1</i>	0.67	0.70	0.70	0.65	0.77	0.77
<i>AR2</i>	0.59	0.65	0.70	0.54	0.73	0.76
<i>CelebA</i>	0.68	0.71	0.73	0.67	0.76	0.76
<i>Average Identity distances</i> (lower the better)						
	(b)	(c)	(d)	GL	GFC	SDG
<i>AR1</i>	0.64	0.61	0.52	0.52	0.48	0.47
<i>AR2</i>	0.75	0.72	0.59	0.67	0.56	0.56
<i>CelebA</i>	0.68	0.62	0.59	0.61	0.55	0.57

7.4. Performance boost in Face Recognition

Face Recognition (FR) systems underperform when the faces are occluded. Our proposed SD-GAN reconstructs a full-face when presented with a occluded face, which facilitates efficient performance for FR. Performances of several recent shallow learning techniques, *viz.* LSM [26], RPCA [27], GL [25] have been compared with our proposed and GFC [6] methods for generation of the faces,

evaluated using state-of-the-art benchmark FR systems, like PCA [28], Gabor [29], LPP [30], Sparse Representation (SR) [4] and VGG [31]. The results in table 2 show the rank-1 accuracies for AR1 and AR2 datasets, where our proposed model (SD-GAN) outperforms all other methods, indicating that it must be capable of generating discriminative parts of the face better than the other competing methods. Interpret the values in the table 2 as performances for FR, for images generated by the methods mentioned at the top of each column, while the FR methods appear at the left of each row. Observe the huge jump in performance from the statistical methods to the GAN based methods, indicating the power of the GAN based techniques for overcoming occluded faces, specifically when applied for FR applications.

Table 2: Rank-1 Recognition rates (in %) exhibiting a higher performance for Face Recognition by SD-GAN (SDG), compared with several state-of-the-art shallow and deep learning techniques on AR Dataset. The results in bold demarcates the best performance (row-wise).

AR1: Recognition of faces with sunglasses						
	Occ.	LSM	RPCA	GL	GFC	SDG
<i>PCA</i>	52.6	61.4	64.2	70.0	82.9	89.7
<i>GPCA</i>	67.5	73.3	71.6	76.6	88.4	93.3
<i>LPP</i>	53.4	45.7	61.4	59.0	83.5	90.1
<i>SR</i>	58.4	59.2	57.3	60.6	85.7	91.6
<i>VGG</i>	84.2	85.4	84.5	87.9	91.7	96.8
AR2: Recognition of faces with scarf						
	Occ.	LSM	RPCA	GL	GFC	SDG
<i>PCA</i>	15.7	37.5	32.2	40.8	72.6	79.4
<i>GPCA</i>	55.1	56.2	54.0	60.9	80.3	88.6
<i>LPP</i>	34.4	43.0	38.3	47.1	75.9	81.2
<i>SR</i>	45.2	51.8	47.7	56.7	79.8	86.8
<i>VGG</i>	72.3	75.9	79.6	83.5	89.9	92.6

An extension of Linear Discriminant Analysis (LDA) [32] to the two color channels I-chrominance and the Red channel (LDA-IR) is described in [32]. Inter-Session Variability (ISV) [32] modeling is a technique that has been successfully employed for face verification, which does not have occluded images during training. The rank-1 recognition rates of the VGG+SD-GAN (VGG is used as a classifier with SDG as the generator), when compared with these two state-of-the-art techniques, LDA-IR and ISV, are much higher for the AR database, as reported in

table 3.

Table 3: Rank-1 Recognition rates for end-to-end system for occluded face recognition. Higher values are better.

Dataset	ISV [32]	LDA-IR [32]	VGG+SDG
AR1	45.13	62.59	96.82
AR2	39.81	57.44	92.64

7.5. Analysis of training time of SD-GAN, compared to GFC [6]

All experiments are performed on a dual GPU machine with dual Nvidia TITAN X, with 64 GB RAM and Intel core i7 4790K processor. The training for both the models are performed using *Keras* with *Tensorflow* backend. The training times are tabulated in table 4, which shows that the SD-GAN is faster than GFC, since it converges near a Nash equilibrium (see arrow on graph in figure 8 for details) in lesser number of epochs as compared to GFC.

Table 4: Comparison of training times of SD-GAN and GFC. Lower value is better.

	AR Face Database		Celeb-A Database	
	#epochs	mins/epoch	#epochs	mins/epoch
GFC	30K	8	20K	25
SDG	550	3	500	12

7.6. Results on the Multi-PIE dataset

In order to evaluate our proposed algorithm on pose-variations of the face images producing self-occlusions, we performed experimentations on MultiPIE dataset, which has 750000+ images, at different poses. Self-occlusion of faces occur due to off-frontal and out-of-plane rotation variations in pose. For evaluating performance using rank-1 recognition rates, we follow the protocol from [33], and only images from session one are used. Results are given in table 5. All images used for testing and validation have 90° pose. Few results shown in figure 9 display the superiority of our method over TP-GAN (TPG) [33], both qualitatively as well as with quantitative measures in terms the SSIM/PSNR values. Observe the sample at the last row of figure 9, which shows a non-frontal (not side profile view) query face. In this case, our result in (c) has produced an exact illumination

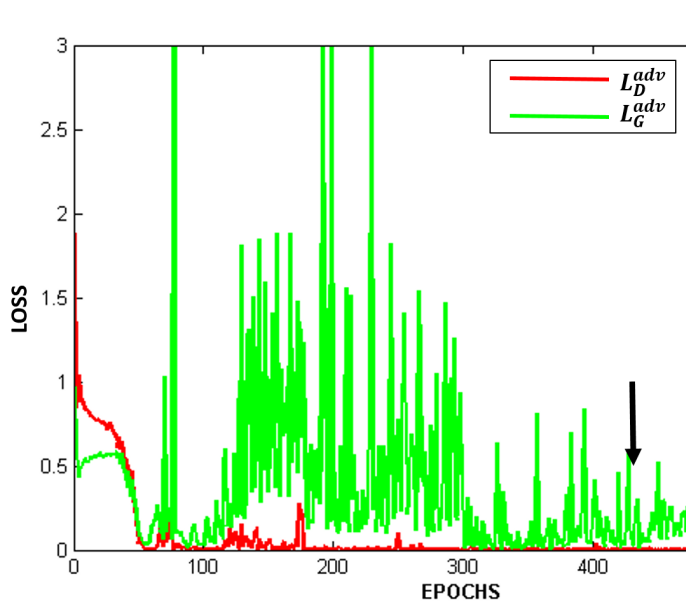


Figure 8: Graphs showing the discriminator and generator loss functions during training.

variation as that in GT (d), whereas the process of [33] in (b) produces exactly the opposite (mirror-like image) while producing a sharper contrast (unnecessarily, in general) than that in GT. Also, observe intriguingly the presence of ear-rings (appears non-identical ones) in the output of [33], not present in GT and our output in (c). The proposed system intrinsically exploits the symmetric nature of the face, helping to generate images with appropriate illumination variations at high-resolution with desired quality as in GT.

Table 5: Comparison of Rank-1 recognition rate for Multi-PIE dataset, with faces at 90° pose (best values are in bold).

Criteria	TPG [33]	SDG
Rank-1 Recognition Rate (%)	64.03	65.19
PSNR	12.26	19.84
SSIM	0.59	0.66

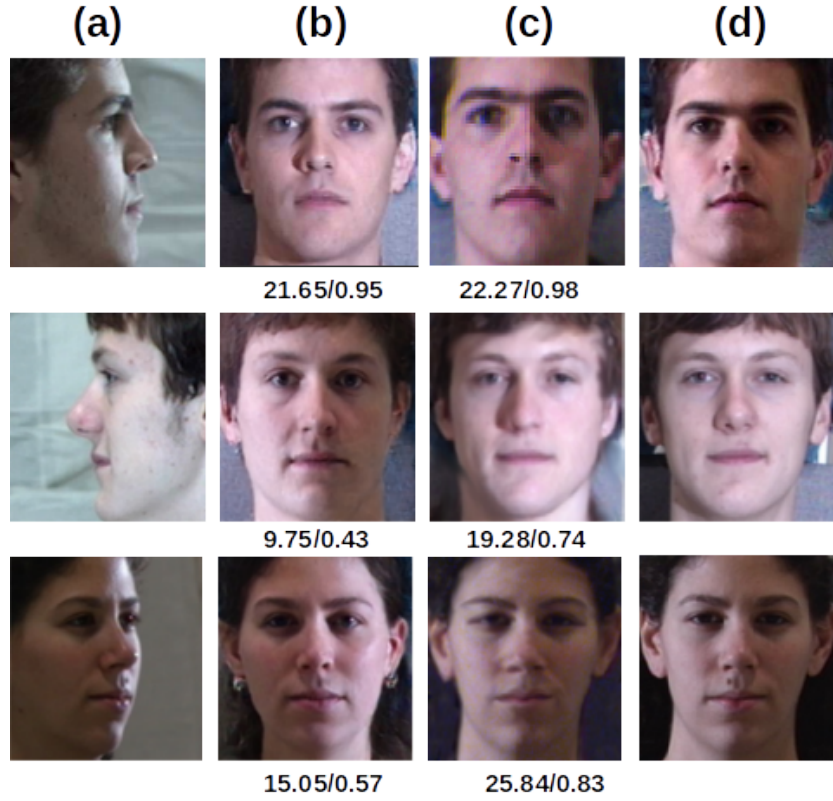


Figure 9: Results for image generation from two different methods: (a) Images at different poses (obtained from Multi-Pie dataset [22], with left- (*top-row*) & right-looking (*Middle-row*) profiles at 90°; and a face image at 60° pose (*Bottom-row*)) used for testing, (b) Image generated by TPG [33], (c) Image generated by SDG, (d) expected output (ground-truth). The values below each image gives the (PSNR/SSIM) values of the image compared to the expected (target) output.

8. Conclusion

The proposed SD-GAN model uses end-to-end training for reconstruction of occluded parts of the face. The proposed technique does not rely on any post-processing technique for semantic correction of the faces. Thus, this module may be used as pre-processing for any FR system, in cases where faces are occluded. A faster training time is ensured in this model, based on the Nash Equilibrium. The qualitative and the quantitative results discussed above confirm the superiority of our proposed model. Misalignment of faces may lead to distortions as happens in all reconstruction techniques. In order to generate better quality photo-realistic images for AR and LFW datasets, the dual pathway technique proposed in [33] can be used as a post-processing stage following our SD-GAN.

References

- [1] I. Goodfellow, J. Pouget-Abadie, M. Mirza, B. Xu, D. Warde-Farley, S. Ozair, A. Courville, Y. Bengio, Generative adversarial nets, in: *Advances in Neural Information Processing Systems (NIPS)*, 2014, pp. 2672–2680. [1](#), [3](#), [6](#), [12](#)
- [2] C. Barnes, E. Shechtman, A. Finkelstein, D. B. Goldman, Patchmatch: A randomized correspondence algorithm for structural image editing, *ACM Trans. Graph.* 28 (3) (2009) 24–1. [2](#)
- [3] J.-B. Huang, S. B. Kang, N. Ahuja, J. Kopf, Image completion using planar structure guidance, *ACM Transactions on Graphics (TOG)* 33 (4) (2014) 129. [2](#)
- [4] J. Wright, A. Y. Yang, A. Ganesh, S. S. Sastry, Y. Ma, Robust face recognition via sparse representation, *IEEE Transactions on Pattern Analysis and Machine Intelligence* 31 (2) (2009) 210–227. [2](#), [18](#)
- [5] J. S. Ren, L. Xu, Q. Yan, W. Sun, Shepard convolutional neural networks, in: *Advances in Neural Information Processing Systems*, 2015, pp. 901–909. [2](#)
- [6] Y. Li, S. Liu, J. Yang, M.-H. Yang, Generative face completion, *IEEE Conference on Computer Vision and Pattern Recognition (CVPR)*. [2](#), [12](#), [13](#), [15](#), [16](#), [17](#), [19](#)
- [7] A. Martinez, R. Benavente, The AR face database, *CVC Tech. Report* (1998) 24. [2](#), [12](#), [13](#)
- [8] Z. Wang, A. C. Bovik, H. R. Sheikh, E. P. Simoncelli, Image quality assessment: from error visibility to structural similarity, *IEEE Transactions on Image Processing (TIP)* 13 (4) (2004) 600–612. [2](#), [5](#)

- [9] A. Krizhevsky, I. Sutskever, G. E. Hinton, Imagenet classification with deep convolutional neural networks, in: *Advances in Neural Information Processing Systems (NIPS)*, 2012, pp. 1097–1105. [2](#)
- [10] P. Vincent, H. Larochelle, Y. Bengio, P.-A. Manzagol, Extracting and composing robust features with denoising autoencoders, in: *Int’l Conference on Machine learning (ICML)*, 2008. [2](#), [4](#)
- [11] J. Schmidhuber, Learning factorial codes by predictability minimization, *Neural Computation* 4 (6) (1992) 863–879. [3](#)
- [12] J. F. Nash, et al., Equilibrium points in n-person games, *Proceedings of the National Academy of Sciences* 36 (1) (1950) 48–49. [3](#)
- [13] Y. Bengio, P. Lamblin, D. Popovici, H. Larochelle, Greedy layer-wise training of deep networks, in: *Advances in Neural Information Processing Systems (NIPS)*, 2007, pp. 153–160. [4](#)
- [14] C. Lee, C. Lee, C.-S. Kim, An MMSE approach to nonlocal image denoising: Theory and practical implementation, *Journal of Visual Communication and Image Representation* 23 (3) (2012) 476–490. [4](#)
- [15] S. Johnson, *Stephen Johnson on digital photography*, O’Reilly Media, Inc., 2006. [6](#)
- [16] A. Radford, L. Metz, S. Chintala, Unsupervised representation learning with deep convolutional generative adversarial networks, in: *International Conference on Learning Representations*, 2015. [9](#), [15](#)
- [17] M. Abadi, P. Barham, J. Chen, Z. Chen, A. Davis, J. Dean, M. Devin, S. Ghemawat, G. Irving, M. Isard, et al., Tensorflow: A system for large-scale machine learning., in: *OSDI*, Vol. 16, 2016, pp. 265–283. [9](#)
- [18] D. P. Kingma, J. Ba, Adam: A method for stochastic optimization, in: *Proceedings of the 3rd International Conference on Learning Representations (ICLR)*, 2014. [10](#)
- [19] S.-i. Amari, Backpropagation and stochastic gradient descent method, *Neurocomputing* 5 (4) (1993) 185–196. [10](#)
- [20] R. Gibbons, *A primer in game theory*, Harvester Wheatsheaf, 1992. [10](#)
- [21] Z. Liu, P. Luo, X. Wang, X. Tang, Deep learning face attributes in the wild, in: *Proceedings of International Conference on Computer Vision (ICCV)*, 2015. [12](#), [13](#), [16](#)

- [22] R. Gross, I. Matthews, J. Cohn, T. Kanade, S. Baker, Multi-pie, Image and Vision Computing (IVC) 28 (5) (2010) 807–813. [12](#), [14](#), [21](#)
- [23] B. Amos, B. Ludwiczuk, M. Satyanarayanan, Openface: A general-purpose face recognition library with mobile applications, Tech. rep., CMU-CS-16-118, CMU School of Computer Science (2016). [15](#)
- [24] P. Pérez, M. Gangnet, A. Blake, Poisson image editing, in: ACM Transactions on graphics (TOG), Vol. 22, ACM, 2003, pp. 313–318. [15](#)
- [25] Y. Deng, Q. Dai, Z. Zhang, Graph laplace for occluded face completion and recognition, IEEE Transactions on Image Processing (TIP) 20 (8) (2011) 2329–2338. [15](#), [17](#)
- [26] B.-W. Hwang, S.-W. Lee, Reconstruction of partially damaged face images based on a morphable face model, IEEE Transactions on Pattern Analysis and Machine Intelligence 25 (3) (2003) 365–372. [17](#)
- [27] J. Wright, A. Ganesh, S. Rao, Y. Peng, Y. Ma, Robust principal component analysis: Exact recovery of corrupted low-rank matrices via convex optimization, in: Advances in Neural Information Processing Systems, 2009, pp. 2080–2088. [17](#)
- [28] M. A. Turk, A. P. Pentland, Face recognition using eigenfaces, in: IEEE Computer Society Conference on Computer Vision and Pattern Recognition (CVPR), IEEE, 1991, pp. 586–591. [18](#)
- [29] Z. Lei, S. Liao, R. He, M. Pietikainen, S. Z. Li, Gabor volume based local binary pattern for face representation and recognition, in: 8th IEEE International Conference on Automatic Face & Gesture Recognition (FG), IEEE, 2008, pp. 1–6. [18](#)
- [30] X. He, P. Niyogi, Locality preserving projections, in: Advances in Neural Information Processing Systems (NIPS), 2004, pp. 153–160. [18](#)
- [31] O. M. Parkhi, A. Vedaldi, A. Zisserman, Deep face recognition, in: British Machine Vision Conference (BMVC), Vol. 1, 2015, p. 6. [18](#)
- [32] M. Günther, L. El Shafey, S. Marcel, Face recognition in challenging environments: An experimental and reproducible research survey, in: Face Recognition Across the Imaging Spectrum, Springer, 2016, pp. 247–280. [18](#), [19](#)
- [33] R. Huang, S. Zhang, T. Li, R. He, Beyond face rotation: Global and local perception gan for photorealistic and identity preserving frontal view synthesis, ICCV, 2017. [19](#), [20](#), [21](#), [22](#)